Advantages of pulse-train excitation in narrow-band terahertz generation: mitigation of undesired nonlinear effects

UMIT DEMIRBAS,[1,2,3] CHRISTIAN RENTSCHLER,[1,4,5] ZHELIN ZHANG,[1,6] MIKHAIL PERGAMENT,[1] NICHOLAS H. MATLIS,[1] AND FRANZ X. KÄRTNER,[1,5,7,*]

[1]*Center for Free-Electron Laser Science CFEL, Deutsches Elektronen-Synchrotron DESY, Notkestr. 85, 22607 Hamburg, Germany*
[2]*Paul Scherrer Institut, CH-5232 Villigen PSI, Switzerland*
[3]*Antalya Bilim University, 07190 Dosemealti, Antalya, Turkey*
[4]*Max Planck School of Photonics, Hans-Knöll-Straße 1, 07745 Jena, Germany*
[5]*Physics Department, University of Hamburg, Luruper Chaussee 149, 22761 Hamburg, Germany*
[6]*Tsung-Dao Lee Institute, Shanghai Jiao Tong University, Shanghai 200240, China*
[7]*The Hamburg Centre for Ultrafast Imaging, Luruper Chaussee 149, 22761 Hamburg, Germany*
**franz.kaertner@desy.de*

Abstract: In this work, we have studied the limitations of narrowband multi-cycle (MC) terahertz (THz) generation via optical rectification (OR) in periodically-poled lithium niobate (PPLN) crystals. Detailed investigation of the transmitted beam profile, THz conversion efficiency (CE), and parasitic second-harmonic generation (SHG) strength as a function of incident pump beam size showed that Kerr-lensing is a significant bottleneck in the efficiency scaling of MC THz generation. We have also demonstrated that compared to the usage of a single pump pulse, excitation of the PPLN crystal via a pulse train, not only boosts up THz CE and narrows down the bandwidth of the achieved THz beam but also helps to mitigate the effect of undesired nonlinearities, such as Kerr-lensing, and parasitic SHG.

1. Introduction

High-energy terahertz sources with low photon energies and long wavelengths are attractive for many applications, from spectroscopy of low-energy excitations in materials [1] to the development of compact electron accelerators [2]. Optical rectification (OR) of ultrashort laser pulses in nonlinear crystals is a well-established technique to generate high-energy THz pulses[3]. Most of the initial studies with THz generation with optical rectification are focused on the generation of broadband single-cycle pulses due to their ability to measure the impulse response of materials with high-peak electric fields. On the other hand, for many applications, resonant excitation via tunable narrowband THz sources has advantages over broadband excitation [4–7]. As a result, there has also been growing interest in the development of tunable narrowband THz sources.

As the nonlinear material for THz generation, organic crystals such as DAST [8,9], DSTMS [10], and OH1 [11] attracted the attention of the community due to their large nonlinear coefficients and low dispersion of refractive index [12–14]. Usually, quite thin samples are used for efficient broadband THz generation, where the temporal walk-off between the THz and pump beams sets the thickness. These thin organic crystal samples generate short (few-cycle) THz pulses with broad spectra, and for longer multi-cycle THz generation, usually the driving pump source is temporally modulated by beating its chirped replicas in Mach-Zehnder or Fabry–Pérot based interferometers (e.g., see Table 1 in [5]). The central frequency of the MC THz pulses could simply be tuned by changing the time delay between replicas of the pump beam. As an example, using DSTMS as the nonlinear medium, broadly tunable narrowband THz pulses with central frequencies in the 0.5-18 THz have been

demonstrated with efficiencies close to 1% [15]. On the other side, THz sources employing organic crystals: (i) usually require pumping at unconventional wavelengths in the 1.2-1.6 μm range [12,14], (ii) have limited tuning ability at low THz frequencies due to strong phonon absorption bands, and (iii) are not suitable for high energy and high-repetition-rate operation, due their fragile nature, low damage threshold, and weak thermomechanical strength [14].

As an alternative material, lithium niobate (LN) also has a high nonlinear coefficient (e.g., see Table 1 in [14]), can be grown in large sizes, possesses strong thermomechanical parameters, and can be pumped by conventional Ti:Sapphire or Yb:YAG amplifiers [16]. For MC THz generation in LN, the velocity mismatch between the optical and THz pulses is exploited: periodically-poled lithium niobate is used for quasi-phase-matched operation [17–19]. Hence, the output of the PPLN crystal is already narrowband, which is an advantage over organic crystals, and pumping with modulated pump pulses (via spatial, temporal, and/or spectral shaping [20–25]) helps to reduce the obtainable bandwidths further. Moreover, the tuning range of MC THZ sources with PPLN covers the ~0.1-3 THz range [26,27], which complements the tuning range obtainable with organic crystals.

For multi-cycle THz generation, numerical studies have shown that the THz conversion efficiency could be improved significantly via exciting the PPLN crystal with pump spectra consisting of a series of narrow lines separated by the resonance THz frequency of the crystal [28,29]. One way to achieve the modulated spectra is via the chirped pulse beating technique, which has been successfully applied to the broadband Ti:Sapphire pump sources [23,30,31]; however, the technique requires precise control of higher-order dispersion to keep the frequency beating constant over the whole spectra. Another approach is demonstrated by temporally chopping and amplifying a pair of single-frequency continuous wave (CW) sources, but this approach is inherently limited since maintaining coherence while combining larger numbers of single-frequency sources in a laser system is rather challenging [24,32]. As the third approach, a regular train of pulses could be obtained in a pulse divider setup in the time domain, which is again equivalent to a multi-line optical spectrum with precise frequency separation in the frequency domain [28].

In our recent work, in pursuit of this third approach, we have shown that a series of polarization-based Michelson interferometers could be used to generate a pump pulse trains with an adjustable pulse number and precisely controllable pulse train repetition frequency [25]. We have further demonstrated that, via tuning the pulse-train parameters, the properties of the generated MC THz pulse could be controlled very accurately, and as a result, THz spectra with record spectral brightness levels could be achieved [25]. It is further shown that scanning the pulse train frequency while recording the THz yield enables the measurement of the frequency response of the PPLN crystal, which enables precise mapping of the key properties of the nonlinear medium [25]. This is first used to estimate the refractive index and absorption coefficient of lithium niobate at 78 K, around the central frequency of 345 GHz [25], then later around 275 GHz as a function of temperature between 78-350 K [33]. On the other hand, at long-term sustainable pump fluences (~100-200 mJ/cm^2), the experimentally obtained efficiencies with PPLN are still around 0.5% level even at cryogenic temperatures [25,33], which is considerably lower than the efficiencies estimated by simple 1-dimensional (1-D) analytical models [25,29]. This discrepancy is illuminated at some level in [25], via comparing experimental and simulation results at several different configurations.

To understand this discrepancy in greater detail, in this follow-up study, we have focused our attention on investigating the undesired effects that could potentially reduce THz CE while generating MC THz pulses in PPLN crystals. This issue has been investigated in some detail for the case of single-cycle THz-pulse generation in LN [34–38], where tilted-pulse-front (TPF) and Cherenkov geometries [39,40] are used for phase matching. Literature showed that effects such as Kerr-lensing (self-focusing) [34,35], multiphoton-induced free-carrier absorption [36,37] and cascading-induced spectral broadening [38] could have a detrimental role in single-cycle pulse generation in LN. These nonlinear processes have the

potential to play a more critical role in MC THz generation. First of all, in MC THZ generation using PPLN, the aperture (transverse size along poling direction) of the commercially available samples is limited to only 4 mm currently; hence, one needs to use more tightly focused pump beams compared to single-cycle THZ generation. Moreover, rather long crystals of several centimeters are employed in MC THz generation to reduce the width of THz spectra, which also intensifies the role of undesired nonlinear processes. Despite these issues, to our knowledge, 2-D and 3-D effects that could limit the THz generation efficiency in MC THz generation in PPLN have not yet been studied in detail.

Motivated by this need, in this work, we have investigated the dependence of THz CE on pump beam diameter in PPLN in great detail. The pulse train excitation approach is used to increase the spectral brightness of the MC THz light. In our study, besides the THz CE that is usually investigated [25], variation of the transmitted pump beam size and parasitic second harmonic generation strength with pump fluence is further investigated to probe the strength of nonlinear effects. Our experimental results have shown that the optimum pump beam diameter for THz generation is significantly larger than what is estimated by simple models, and we have identified the Kerr-lensing (self-focusing) mechanism in PPLN as a strong candidate for this discrepancy. Furthermore, we have shown that by exciting the PPLN crystal with a pulse train, besides improving the THz conversion efficiency and THz spectral brightness, one can also mitigate the undesired nonlinear effects such as Kerr-lensing and parasitic SHG. We hope that the experimental findings in this work are a first step in a thorough investigation of 2-D and 3-D effects in MC THz generation in PPLN, and our findings can be used to better understand and improve the performance of MC THz generation.

The paper is organized as follows: In Section 2, we briefly outline our experimental methodology. In Section 3, we present experimental results on variation of THz CE, parasitic SHG, and self-focusing with pump beam spot size and pulse burst length. Section 4 provides a brief conclusion of the results, whereas in the Appendix (Section 5), we present supplementary details.

2. Experimental Setup

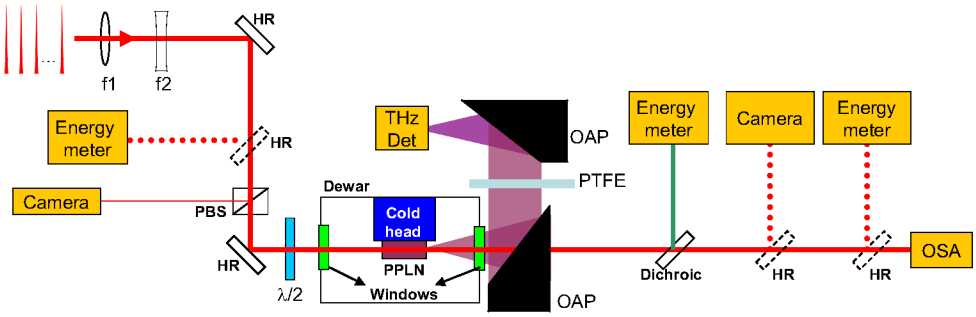

Fig. 1. Schematic layout of the THz generation and detection setup used in the experiments. OAP: Off-axis parabola, OSA: Optical spectrometer, HR: Pump high-reflector.

For the experiments, a home-built laser system consisting of a seeder, a regenerative amplifier (regen), and a multi-pass amplifier was developed as the pump source for THz generation. The system has been recently introduced in detail in [25] and [33], so here, our discussion will be quite brief (e.g. see Fig. 1 in [25]). An optical pulse divider setup consisting of seven sequential polarization-based Michelson interferometers is used to generate a pulse train with an adjustable number of pulses between 1 (2^0) and 128 (2^7). In each Michelson interferometer, the input pulses are copied, and one copy is delayed in time by a certain amount using a motorized delay stage to attain a train of regularly spaced pulses. The

motorization allows precise tuning of the temporal spacing of the pulses, and the regularity of the pulse train is confirmed via several methods (e.g., see Section 3.2 in [25], and Section 5.1 in [33]). The pulse train is amplified to up to 30 mJ at 10 Hz repetition rate, and the individual pulses are compressed down to 800 fs. The size of the pump beam can be adapted freely using a tunable telescope (f1 and f2 in Fig. 1). For THz generation, the infrared pulse trains are directed to a PPLN crystal in a cryostat, which can be cooled down to 78 K to minimize THz absorption in the material[33]. The congruently grown, 5% magnesium oxide (MgO) doped PPLN crystal had a poling period of 400 μm, an aperture of 4x4 mm^2, and a length of 20 mm and is the same sample used in [33] (crystal contains N_{PPLN}=50 (20/0.4) poling periods, N_{PPLN} as defined in [25]). Note that the 4 mm aperture is currently the largest that could be commercially obtained, which necessitates a smaller beam size on these samples.

The THz radiation is generated collinearly with the laser beam. The pump beam and the THz radiation polarization were both parallel to the extraordinary axis of the lithium niobate crystal, which was in vertical orientation (hence both the pump and the THz beams were s-polarized). The PPLN crystal also produced parasitic second harmonic light, which was also s- polarized. The generated THz beam is collected and focused onto a THz detector by a pair of 10 cm focal length, 2-inch off-axis parabolas (OAPs) with a protected gold coating. A 1 cm thick Teflon slab (PTFE) was inserted between the two OAP mirrors to block the remaining pump beam entirely. The first OAP mirror had a 3 mm wide through-hole to allow passage of most of the pump beam, which is then used to characterize the changes in the beam profile and spectral content of the transmitted pump beam. A 45-degree dichroic beam splitter (highly transmissive around 1030 nm and highly reflective around 515 nm) is further used to direct the generated parasitic second harmonic (green) light in another direction to investigate its properties (energy, spectrum, etc.).

The THz energy is measured using a pyroelectric detector with a sensitivity as low as 20 nJ (Gentec SDX-1152 with a 9 mm diameter active area). The calibration of the THz detector is performed in-house by comparing its reading with a calibrated sensor from Lasertechnik GmbH (THz 20, calibration certificate 73426 PTB 18, owns a flat frequency response across the 0.1–3 THz range) [40,41]. The infrared and green pulse energies are measured with calibrated pyroelectric energy sensors (Coherent, EnergyMax-RS J-25MB-LE and EnergyMax-RS J-10MB-LE) with measurement ranges of 50 μJ to 50 mJ, and 0.5-600 μJ and sensitivities of 5 μJ and 50 nJ, respectively.

3. Results and Discussions

3.1 THz and parasitic second harmonic generation efficiency as a function of burst length (pulse number)

In our earlier work [25,42], we have already investigated the variation of THz conversion efficiency with the number of pulses in the pulse train (N_{train}) in some detail, for pulse numbers between 32 and 256. Here, we will look at variations of THz CE as well as parasitic second harmonic (or green) generation efficiency as a function of pulse number for pulse numbers of 2, 4, 8, 16, 32, 64, and 128. The parasitic second harmonic process is not phase-matched in the PPLN crystal used; however, we have seen in our experiments that, even if it is not phase-matched, it can be as strong as the THz beam, and its strength is an indication of the undesired nonlinearities in the PPLN crystal. Parasitic SHG not only reduces the strength of the pump beam, but it could also induce infrared absorption in PPLN [43,44]. Hence, the strength of the parasitic SHG light is also investigated here.

In Figs. 2 (a) and (b), we plot the variation of internal THz energy and the generated green energy as a function of the total pump energy of the pump pulse bursts. The pulse bursts used contained different numbers of pulses between 2 and 128. In Fig 2 (a), by internal THz energy, we mean the estimated energy at the end of the PPLN crystal, so we consider the losses of the PPLN exit surface, dewar windows, and Teflon filter, and a detailed account of

this can be found in Table 1 of [25]. For the specific case presented here, the external energy measured on the detector is about 3 times lower than the estimated internal THz energy. This approach is used to easily compare the results taken in different geometries/temperatures, and the validity of the internal energy estimate is confirmed by investigating the spectral shift of the pump beam (a detailed account of this can be found in the Appendix, Section 5.1).

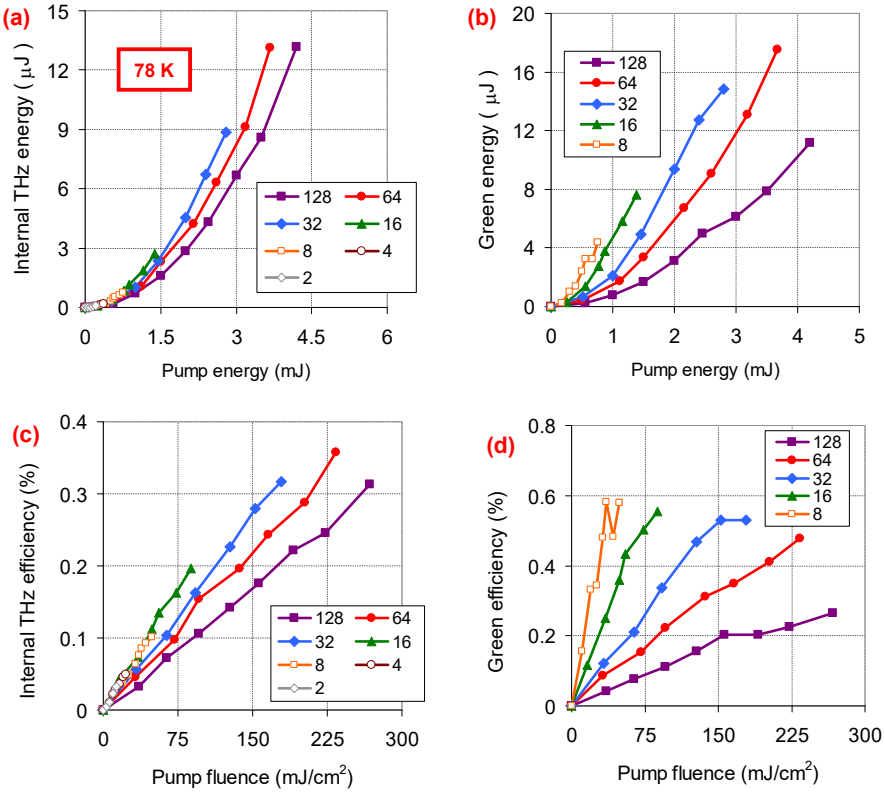

Fig. 2. Measured variation of (a) internal THz and (b) parasitic SH (green) energy as a function of incident pump energy. Measured variation of (c) internal THz and (d) green efficiency as a function of pump fluence. The data is taken at cryogenic temperatures (78 K), with the 2 cm long PPLN crystal with a QPM period of 400 μm, using a 2 mm diameter input pump beam, while using pulse bursts, with pulse numbers between 2 and 128. The pulse train frequency is set to 286 GHz, which is the resonance frequency of the 400 μm poled PPLN at 78 K [33].

From Fig. 2 (a), we see that the internal THz energy only weakly changes with the number of pulses in the pump burst, and only a slight decrease with pulse number is observed. In the case of parasitic SHG/green energy (Fig. 2 (b)), we clearly see that, at increased burst lengths (increased pulse numbers), the energy converted to green decreases considerably. When we look at the THz generation and parasitic green efficiency as a function of total pulse peak fluence (Fig. 2 (c-d)), we see a similar trend. For the generated THz, we do not see a big variation, but for the case of the parasitic green, we see a sharp decrease in efficiency with increasing pulse number. It is educational to look at this phenomenon in more detail to understand the different behaviors of THz and parasitic second harmonic generation processes.

For that purpose, in Fig. 3 (a) and (b), we now plot the THz and parasitic SH efficiency curves in terms of energy per pump pulse in the burst (so to obtain these graphs, we have

divided the measured energies in Figs. 2 (a)-(b) to $N_{train,}$ the number of pulses in the train). This enables us to observe the contribution of each pulse in the burst. Similarly, in Fig 3 (c) and (d), we plot the calculated THz generation and parasitic green efficiencies as a function of peak fluence per pulse (or peak intensity of the individual pulses). It is easier to understand the trend in parasitic green generation, so we start from it. We clearly see from Fig 3 (b) and (d) that, for a fixed pump energy per pulse or fixed peak fluence/intensity per pulse, the obtained green efficiency is the same within experimental error bars, and it is independent of the pulse number used in the bunch. This is rather expected; basically, for the SH generation process, there is no coherent build-up of the SH fields generated by the individual pulses in the train, as the frequency of the pulse train is not in resonance with the SH generation process [45]. Another way to think about this is that the SHG from each pulse is temporally distinct from the SHG of other pulses, and hence, the SHG pulses do not overlap and so do not feel any effects from each other.

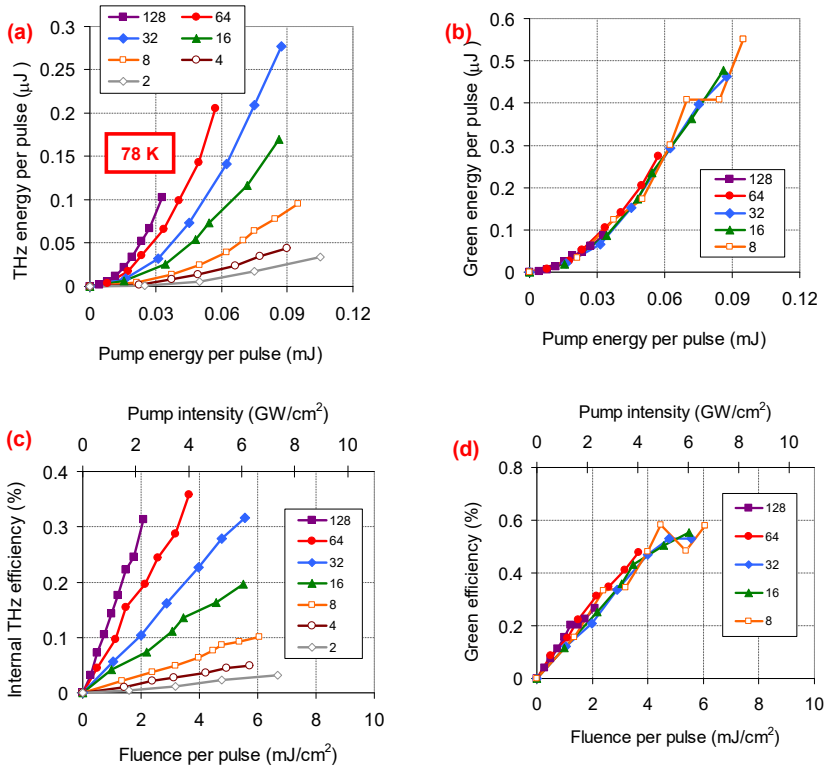

Fig. 3. Measured variation of (a) internal THz energy per pulse and (b) green energy per pulse as a function of pump energy per the individual pulse in the pulse burst. Measured variation of (c) internal THz CE and (d) parasitic green CE as a function of pump fluence per pulse (or peak intensity of the individual pulses). The data is taken at cryogenic temperatures, with the 2 cm long PPLN crystal having a QPM period of 400 μm, using a 2 mm diameter ($1/e^2$) input pump beam and pulse bursts with pulse numbers of 2, 4, 8, 16, 32, 64, and 128.

To understand it better, let us consider the case where a single pump pulse, with an energy of E, pumps the PPLN crystal. Assume that the single pulse generates a parasitic green pulse with an efficiency of η, and hence the output green pulse has an energy of ηE (Table 1). Now, as the second case, we excite the same crystal with a pulse train with N pulses, each with an energy of E/N, and hence the total energy of the pulse train is still E. Then, we know from the experimental results presented in Fig. 3 (d) that the mechanism for SH generation is not a resonance process and the parasitic green efficiency scales with the fluence (or peak

intensity) of individual pulses (note that assuming an even pulse train, the peak intensity of the pulse train is the same as the peak intensity of individual pulses). In such a case, we expect that each pulse in the pump burst, with an energy of E/N, will generate green pulses with an efficiency of η/N (as the process scales with fluence). Then the pulse train will generate N green pulses, each with an energy of (E/N)(η/N)=ηE/N^2, and the total energy of the green pulse burst will be Eη/N. By this simple analysis, we clearly see that the generated parasitic green energy will roughly scale as 1/N, which is what we have observed in Fig. 2 (b). From this basic analysis and the measured trend in Fig. 2, it is pretty clear that, the usage of the pulse train suppresses the effect of any non-resonant process, including the parasitic second harmonic generation. In the coming sections, we will show that the pulse train approach is also effective in reducing other undesired nonlinearities. We refer the reader to Section 5.2 in the Appendix for further information on the parasitically generated SH light, such as its spectral content, non-resonant behavior, and temperature dependence of its strength.

Table 1: Estimation of the scaling of the parasitic SH generation efficiency with the number of pulses in the burst. The analysis assumes that the SH efficiency scales with the peak intensity/fluence of pump pulses.

Pulse number	Total pump burst energy	Pump energy per pulse	Peak pump fluence	SH generation efficiency	SH energy per pulse	Overall SH generation efficiency
1	E	E	F	η	ηE	η
2	E	E/2	F/2	η/2	ηE/2^2	η/2
N	E	E/N	F/N	η/N	ηE/N^2	η/N

In the case of THz conversion efficiency, understanding the observed trend requires a more detailed look, as the pulse train excitation frequency is in resonance with the THz frequency of the PPLN crystal, and hence, the resulting behavior is quite different. We see from Fig. 3 (a) that, for a fixed energy per pulse, the THz energy produced per pulse is actually higher when the pulse number is increased. From a similar perspective, Fig. 3 (c) shows that the THz CE is increasing with the increasing number of pulses. To understand this behavior, one needs to look into the analytical model that is developed in [25] for resonance excitation of MC THz generation via a pulse train. As it is described earlier [25,28,29], the efficiency in MC THz generation depends on both the properties of the optical drive laser as well as the properties of the nonlinear crystal used for THz generation and can be modeled as:

$$\eta_{THz} \approx \int_{-\infty}^{\infty} g_{PPLN}(\Omega)\, x\, g_{opt}(\Omega)\, d\Omega. \quad (1)$$

In Eq. 1, $g_{PPLN}(\Omega)$ is the frequency response of the PPLN crystal, and $g_{opt}(\Omega)$ represents the THz excitation spectrum of the pump pulse (available spectrum for the nonlinear processes). For the case of negligible absorption, the frequency response of the PPLN crystal could be described by the well-known Sinc function as it derived in [25]:

$$g_{PPLN}(\Omega) = Sinc^2\left[\pi N_{PPLN}\frac{\Omega-\Omega_{PM}}{\Omega_{PM}}\right]. \quad (2)$$

In Eq. (2), N_{PPLN} is the number of poling period and $\Omega_{PM}$is the phase-matched angular frequency of the PPLN crystal. The FWHM relative bandwidth ($\Delta\Omega_{FWHM}/\Omega_{PM}$) introduced by the PPLN crystal could then be estimated using ~$0.89/N_{PPLN}$ [25], which is around ~1.8 % (~5.1 GHz) for the crystal at hand (20 mm long PPLN with a QPM period of 400 μm, corresponding to a N_{PPLN} of 50 and a central THz frequency of 286 GHz at 78 K [33]). Note that this bandwidth increases to around 5% at room temperature due to the broadening effect of absorption (see Eq. 4 in [25]).

From Eq. (1), the efficiency of THz generation also depends on the properties of the optical drive laser. The THz-excitation spectrum associated with the optical driver could be calculated using [25]:

$$g_{opt}(\Omega) = \mathrm{Exp}\left[-\frac{1}{2}(\Omega\Delta t)^2\right] Sinc^2\left[\pi N_{train}\frac{\Omega-\Omega_{train}}{\Omega_{train}}\right]. \quad (3)$$

In Eq. (3), Δt is the 1/e duration of the individual pulses in the pulse train (the FWHM pulse duration is 1.665xΔt), N_{train} is the number of pulses in the train, and Ω_{train} is the frequency of the pulse train, which is chosen as Ω_{PM} for on-resonance excitation (~286 GHz for the PPLN sample at hand at 78 K).

To better illustrate the issue, in Fig. 4 (a), we show the calculated acceptance bandwidth of our PPLN crystal (ignoring absorption), as well as the THz-excitation spectrum associated for the pulse train, for pulse numbers between 1 and 128. We see that, the available spectrum for nonlinear process (THz generation) of a single 800 nm pulse (FWHM) covers a very broad spectral region, much broader than the acceptance bandwidth of the PPLN crystal. In general, the FWHM relative bandwidth ($\Delta\Omega_{FWHM}/\Omega_{train}$) of the THz-excitation spectrum of the pump could also be estimated using a similar formula: ~$0.89/N_{train}$ [25].

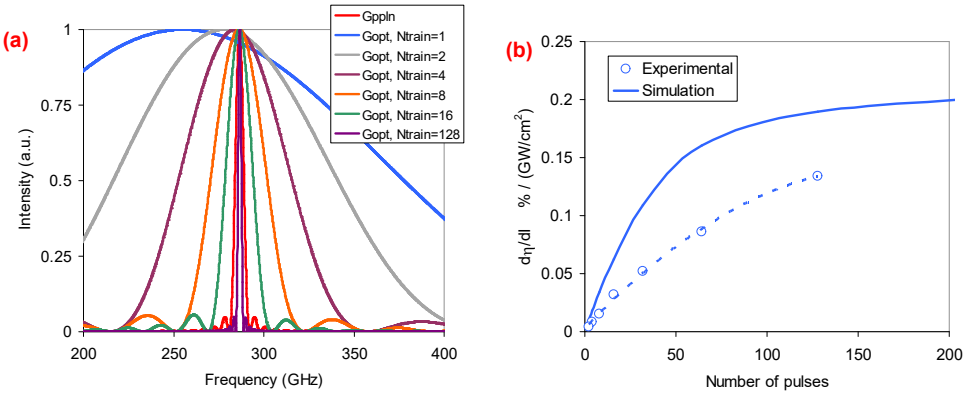

Fig. 4. (a) Calculated THz acceptance spectrum (g_{PPLN}) of 2 cm thick PPLN crystal with a QPM period of 400 μm at 78 K, ignoring THz absorption. Calculated variation of THz excitation spectrum of the pulse burst (g_{opt}) with pulse number, for pulse numbers between 1 and 128. The calculation has been performed for a pulse train frequency of 286 GHz and a pulsewidth of 800 fs (FWHM). (b) Calculated and measured variation of THz CE with pulse number (here THZ CE per pump pulse peak power (dη/dI) is shown). The experimental data is the average slope efficiency for each curve in Fig. 3 (c).

We see from Fig. 4 (a) that, when a pulse train at the correct repetition frequency (~286 GHz) is formed, the laser pump pulse THz excitation spectrum, which is centered around the PPLN phase matching central frequency, gets narrower as the number of pulses in the train is increased. For the specific case studied here, a pulse burst with 4 pulses has an excitation spectrum with an FWHM of around 60 GHz (~0.89*286/4), and this width reduces to 15 GHz with 16 pulses, and to around 4 GHz with 64 pulses (and becomes narrower than the acceptance bandwidth of the PPLN crystal at hand). Hence, as the excitation spectrum of the optical driver matches the acceptance bandwidth of the PPLN better, the THz generation efficiency is first expected to increase linearly with the number of pulses in the train. Then, once the excitation spectrum is narrow enough, the efficiency should level-off. The trend of the simulation curve in Fig. 4 (b) basically shows the above-described trend in THz CE [25]. Note that, in Fig. 4 (b), in accordance with our earlier work [25], we have chosen to plot the slope of THz CE with respect to peak intensity of the pump burst (dη/dI: an intensity-based performance metric for THz CE [25]). The measured experimental variation of THz CE per peak intensity of the pump pulses is also shown in Fig. 4 (b) (the experimental points are the

average slope of the efficiency curves in Fig. 3 (c)). We see that the experimental results are lower than the predicted efficiencies for all pulse numbers. Moreover, there is a reasonable agreement between the trend of the simulation curve and the trend in experimental data, as was the case in [25]. Overall, our measurements in this section showed that the pulse-train excitation approach improves THz CE and suppresses the parasitic SHG strength, a two-fold advantage in MC THZ generation with PPLN crystals.

Before we close this section, we would like to emphasize that the number of pulses in the pulse train not only affects the THz efficiency but also modifies the bandwidth of the generated THz spectrum. At cryogenic temperatures, ignoring THz absorption, excitation with a single pump pulse generates a MC THz beam with N_{PPLN} cycles (50 for the crystal at hand). When the crystal is excited with a pulse train with N_{train}pulses, the THz field initially gets longer in the time domain for small number of pulses, and the system generates a THz beam with $N_{PPLN} + N_{train} - 1$ cycles. However, once the pulse length of the pulse train becomes as long as the crystal length, or in other words, once the pulse train fills the PPLN crystal ($N_{train} \geq N_{PPLN}$), the increase in the THz pulsewidth starts to saturate, similar to the saturation observed in THz conversion efficiency, as we have just outlined above. Because of this effect, the pulse train excitation could be used to produce MC THz pulses with record spectral brightness. The picture outlined above ignored THz absorption; however, since the PPLN crystal possesses some level of THz absorption even at cryogenic temperatures, the absorption will effectively limit the brightness of the THz spectra that could be achieved.

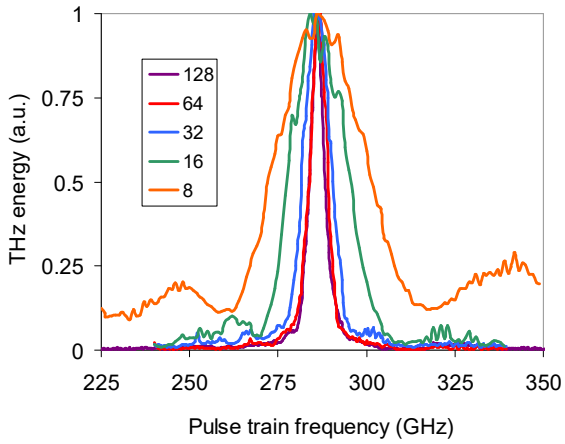

Fig. 5. Measured THz energy as a function of the periodicity of the pulse train for pulse bursts with pulse numbers of 8, 16, 32, 64, and 128.

As outlined in [25], a major advantage of the pulse-divider approach is the ability to map out THz efficiency precisely as a function of pulse-train frequency. In this approach, one can experimentally measure the frequency response of the PPLN crystal via scanning the pulse train frequency and recording the THz energy at different THz frequencies ($\eta_{THz}(\Omega_{train})$). The resulting curve, "tuning curve", provides information about the phase-matching spectrum of the PPLN crystal. Mathematically, the tuning curve measures a convolution of the frequency response of the PPLN crystal ($g_{PPLN}(\Omega)$), and the THz-excitation spectrum associated with the optical driver $g_{opt}(\Omega)$ [25]:

$$\eta_{THz}(\Omega_{train}) \sim \int_{-\infty}^{\infty} g_{PPLN}(\Omega) g_{opt}(\Omega) d\Omega \,. \quad (4)$$

We can see from Eq. 4, that for pulse train excitation with a large number of pulses, the THz-excitation spectrum associated with the optical driver could become very narrow (compared to the acceptance bandwidth of the PPLN crystal), and then the tuning curve effectively

measures $g_{PPLN}(\Omega)$ [25,33]. In the opposite case, when the system is excited with a single pump pulse, the phase-matching spectrum of the PPLN crystal could be much narrower than the THz-excitation spectrum associated with the optical driver, and the convolution provides information about the properties of the pump laser. For cases in between, a deconvolution should be performed to estimate the width of the THz spectrum generated by the PPLN crystal.

Fig. 5 shows the measured tuning curve of the PPLN crystal at 78 K while exciting the sample with a pulse burst with pulse numbers between 8 and 128. We can see from Fig. 5 clearly that the center frequency stays around 286 GHz in all cases, showing that this is the primary THz frequency generated for all pulse bursts. Moreover, as the number of pulses in the pulse train is increasd, the measured tuning curve gets narrower. As described above (Eq. 4), one can then use the measured tuning curves (convolution curves) to estimate the spectral bandwidth (FWHM) of the generated THz beam. With this approach, we have estimated the bandwidth of the generated THz beam as 4.5 GHz, 5.5 GHz, 6.6 GHz for pulse train numbers of 128, 64, and 32, respectively. For lower pulse numbers, the length of the PPLN crystal dominates and determines the width of spectra, which we estimate to have a width of around 8 GHz at 78 K.

3.2 THz and parasitic SHG efficiency as a function of pump beam size

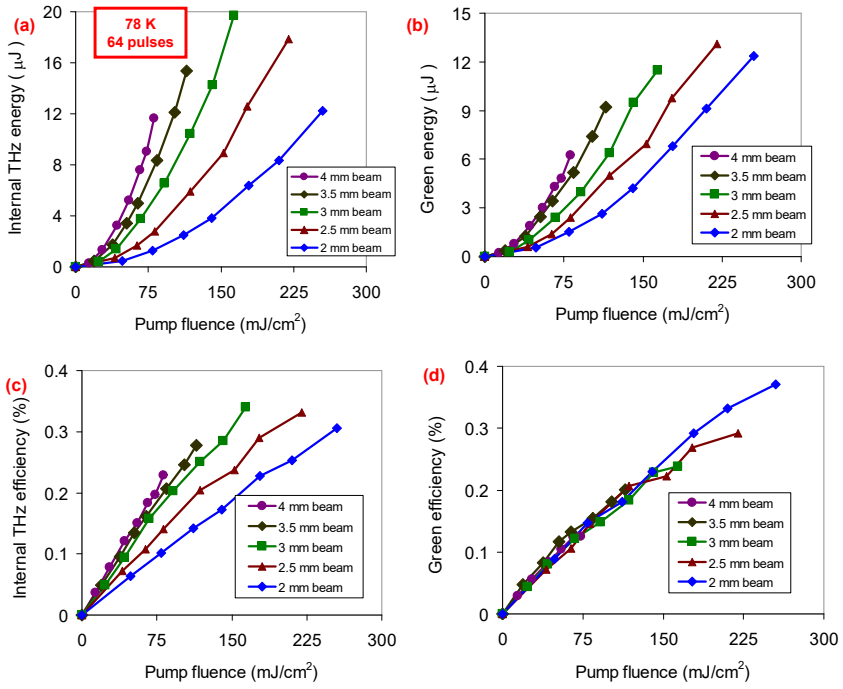

Fig. 6. Measured variation of (a) internal THz energy (b) parasitic second harmonic (green) energy, (c) internal THz CE, and (d) green efficiency at different pump beam diameters. The data is taken at cryogenic temperatures, with the 2 cm long PPLN crystal with a QPM period of 400 μm, using a pulse train with 64 pulses. The pulse train frequency is set to 286 GHz, which is the resonance frequency of the 400 μm poled PPLN at 78 K [33].

In this subsection, we will summarize our efforts in determining the optimum pump beam focusing conditions on MC THz generation with PPLN. The experiments are performed using pulse trains to benefit from the efficiency advantage, as outlined in the earlier section. To start our discussion, in Fig. 6, we show the measured variation of THz CE and the undesired

parasitic SHG efficiency at 78 K for different pump beam diameters ($1/e^2$) between 2 mm and 4 mm. Note that, for the large beams, the PPLN crystal, which had an aperture of 4 mm x 4 mm, there is some loss due to aperture effects, and the energy loss of the pump beam due to the aperture has been considered in the analysis. If we again start from the green efficiency (Fig. 6 (d)), which is easier to understand, we see that the parasitic second harmonic generation efficiency per pump fluence is independent of the pump beam size. This is expected, as the Rayleigh range of the parasitically generated second harmonic light (~515 nm) in the PPLN crystal (>3 m for a beam diameter of 1 mm) is much longer than the PPLN crystal length (20 mm) used in this study.

On the other hand, we see that the THz generation efficiency increases considerably with increasing beam size (Fig. 6 (c)). For the central THz frequency at hand (286 GHz), the wavelength of the THz beam in air is around 1.05 mm, and for the 2 mm diameter pump beam, assuming a THz beam size same as the pump beam size, the Rayleigh length is around 3 mm in air, and around 14.4 mm inside PPLN crystal. It is clear that, if the Rayleigh length of the THz beam is much shorter than the crystal length, the overlap of the THz beam with the pump beam will get worse, and this will reduce the seeding efficiency of the THz that is generated in earlier sections of the crystal and will eventually reduce the overall THz CE. Secondly, for a very tightly focused infrared beam, not all the transverse Fourier components will be phase-matched, and hence, the conversion efficiency will drop, and the transverse profile of the THz beam will deteriorate (at the extreme, the generated THz beam could get a cone-shaped (annular) beam profile [46,47]). Basically, the generated THz beam will have a very large divergence angle for a very tightly focused pump beam, and only a small part of the different Fourier components of the THz beam in this large cone could be phase-matched due to the limited acceptance bandwidth of the crystal in the Fourier domain. Moreover, the transmission of the generated THz beam across the PPLN boundary will drop, and it will effectively fall to zero at the total reflection angle, which is only around 11.35° for the LN to air interface at 78 K [46–48]. Note that, due to the total internal reflection process, the PPLN crystal acts as a waveguide to the THz beam (like a fiber), and the size of the THz beam that exits the PPLN crystal does not depend on the pump beam diameter. Hence, the measured decrease in THz conversion efficiency with tight focusing of the pump beam is not due to a change in the collection efficiency of the THz measurement setup. For more information on this issue, we refer the reader to the Appendix (Section 5.4).

As the strength of these effects depends on the length of the nonlinear crystal used, to compare different experimental conditions (to eliminate crystal length dependence), it is helpful to define a focusing parameter (ξ) as crystal length over confocal parameter [47,49]:

$$\xi = \frac{L}{2\,z_R} = \frac{\lambda_{THz}\,L}{2\,\pi\,n_{THz}\,w^2}\,. \tag{5}$$

In Eq. 5, L is the length of the nonlinear crystal, z_R is the Raylength range of the THz beam, λ_{THz} is the THz wavelength, n_{THz} is the THz refractive index, and w is the pump beam size. Earlier work by Vodopyanov [47] suggests that taking $\xi = 1$ is a good compromise between efficiency and beam profile (in such a case, the crystal length is as long as the confocal length of the THz beam), which makes rather sense. For our 20 mm crystal, a Rayleigh range of 10 mm should then provide a fair optimum point, which suggests the usage of a pump beam diameter of around 1.65 mm. Note that this is in contradiction with what we have measured experimentally, as our THz CE using a 2 mm diameter pump beam was rather low, and we roughly observed a doubling in efficiency when we switched to a pump beam diameter of 4 mm (this corresponds to a ξ of around 0.17). This basically shows that beyond the problems considered in [32–34] (out-coupling of the THz beam across the exit surface of the crystal and phase matching with different transverse components of the pump beam), we have other mechanisms present in our system affecting the THz CE. In the next section, we will show that self-focusing provides a tighter limit than what is considered earlier in optimizing the beam focusing parameter on MC THZ generation in PPLN.

Before we pass on to the next subsection, we note here that, due to the lower damage threshold of PPLN at cryogenic temperatures, the pump fluences we applied are kept below 250 mJ/cm^2 (Fig. 6). To see the variation of THz and parasitic second harmonic generation efficiency at higher fluences, we have repeated the beam size dependence of THz CE variation also at room temperature, where we have applied peak fluences up to 1 J/cm^2 (Fig. 7). In the room temperature data, the pump beam diameter is varied between 1.25 mm and 4.5 mm. We can clearly observe that, as expected, the THz CE is much lower (20-fold) compared to the data taken at 78 K due to the strong THz absorption at room temperature [33]. On the other hand, the parasitic SHG efficiencies are higher due to the larger fluences that are applied. In general, the measured change of performance with beam size is similar to the data taken at 78 K: (i) within experimental errors, the green generation efficiency is independent of beam size, and (ii) THz CE improves using larger beam sizes. However, the room-temperature data taken at higher fluences also shows that both the THz and the parasitic green efficiency start to saturate (and even roll over), indicating a problem with the pump beam at these fluences. Furthermore, when we investigated THz and green efficiency at room temperature for PPLN crystals with lengths of 10 mm, 20 mm, and 40 mm, we saw that the saturation behavior starts earlier with the long crystals, which indicates that the influence of this effect on the pump beam is stronger in longer crystals (see Appendix Section 5.3). All of these together hint that the self-focusing of the pump beam is the cause of this problem, and this will be elaborated on in detail in the next section.

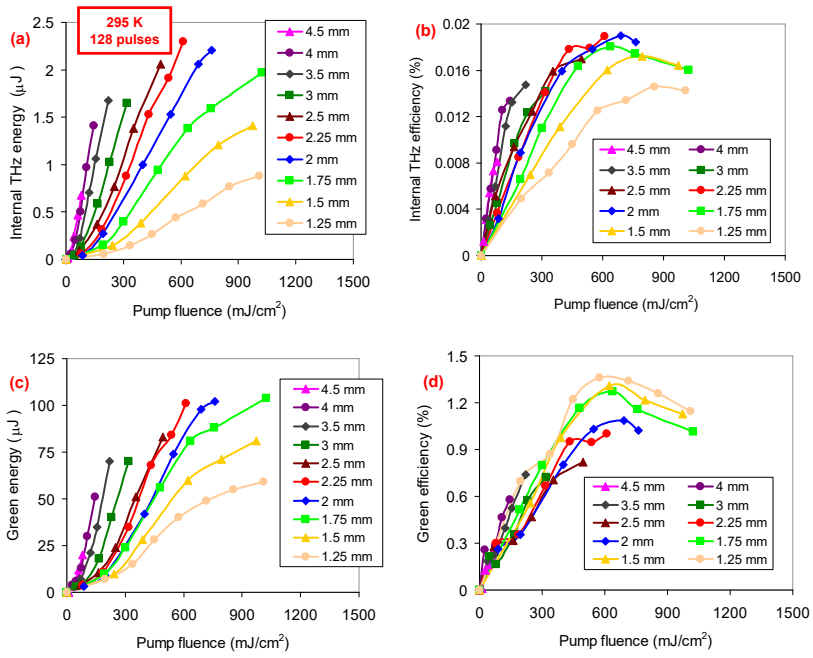

Fig. 7. Measured variation of (a) internal THz energy and (b) internal THz CE, (c) parasitic second harmonic (green) energy, and (d) green efficiency at different pump beam diameters. The data is taken at room temperature (~295 K), with the 2 cm long PPLN crystal with a QPM period of 400 μm, using a pulse train with 128 pulses. The pulse train frequency is set to 262 GHz, which is the resonance frequency of the 400 μm poled PPLN at 295 K [33].

3.3 Self-focusing effect in PPLN as a function of pump burst length (pulse number)

As the next step, to understand the observed behavior of THz CE and parasitic SHG efficiency as a function of pump beam diameter and pulse number, we have studied the

transmitted pump beam profile behind the nonlinear crystal at different pump-fluence values and for different numbers of pulses in the pulse burst. The data is taken at room temperature as it allows the application of larger fluences. Fig. 8 shows the measured variation of the transmitted pump beam profile (after around 1 m from the end surface of the PPLN crystal) with pump peak fluence for a pulse train with (a) 16 and (b) 128 pulses, respectively. We see that the shape of the optical pump beam behind the crystal changes significantly as the peak fluence of the pulse train is increased from around 1-5 mJ/cm^2 to 800 mJ/cm^2. Note that, at high fluences, a low-intensity halo around the strong central part is visible (Fig. 9), which is a typical indication of Kerr-lensing.

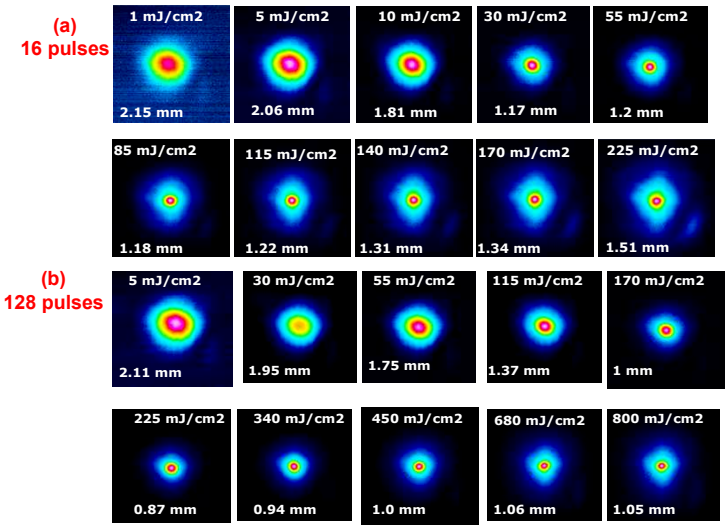

Fig. 8. Measured variation of transmitted pump beam profile as a function of incident fluence while exciting the PPLN crystal with a pulse train with (a) 16 and (b) 128 pulses. The data is taken at room temperature, with the 2 cm long PPLN crystal with a QPM period of 400 µm, using an incident pump beam diameter of 2 mm.

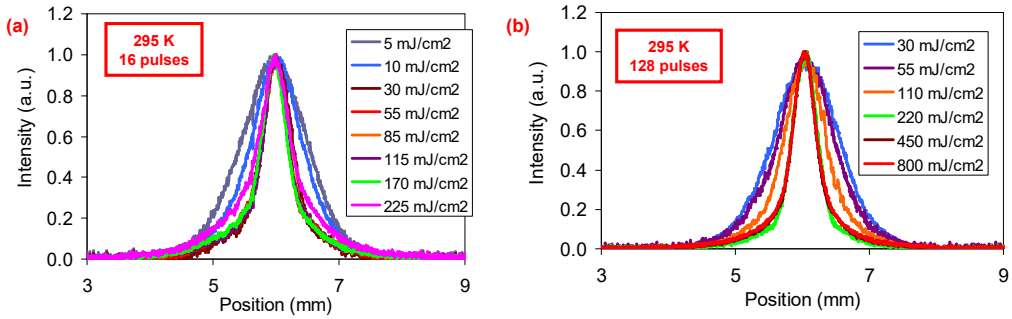

Fig. 9. Measured variation of transmitted pump beam profile in the horizontal axis as a function of incident fluence while exciting with a pulse train with (a) 16 and (b) 128 pulses.

Basically, the transmitted pump beam shows a drastic change in shape and size at high fluence levels due to the Kerr nonlinearity of lithium niobate. The nonlinear refractive index of LN is actually rather small (9.1x 10^{-20} m^2/W [50]) among the other alternatives for THz generation, such as GaAs, ZnTe, and GaP [45], but it is still 3-4 times larger compared to fused silica. Note that, one big difference for pulse trains with 16 and 164 pulses is that the Kerr effect is much more substantial for the pulse train with 16 pulses. As an example, at the

fluence level of 55 mJ/cm^2, the beam diameter is already reduced from 2.15 mm to 1.2 mm level for 16 pulses. In contrast, the beam diameter is only reduced from around 2.11 mm to 1.75 mm for the case of 164 pulses. This is expected since as the number of pulses in the train increases, the peak fluence per pulse or the peak intensity of the individual pulses decreases, and the Kerr effect, which linearly scales with peak power, is reduced (see Eq. 10 in Appendix Section 5.6).

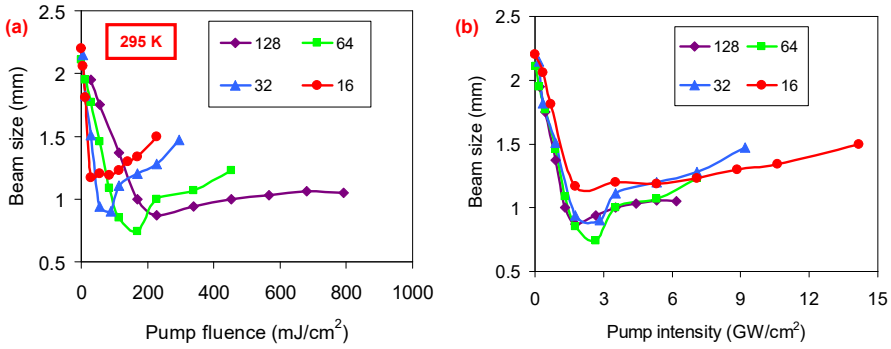

Fig. 10. Measured variation of pump beam diameter (1/e^2) of the transmitted optical beam after the PPLN crystal at room temperature as a function of (a) pump burst peak fluence (total fluence of the burst) and (b) pump burst peak intensity. The data is taken for pulse bursts with pulse numbers of 16, 32, 64 and 128 pulses, at room temperature, with the 2 cm long PPLN crystal with a QPM period of 400 μm, using a pump diameter of 1.5 mm.

In Fig. 10, we summarize the results taken with 16, 32, 64 and 128 pulses. Fig. 10 (a) shows the variation of transmitted pump beam size for different burst lengths as a function of the total fluence of the pulse. We see from Fig. 10 (a) that, in the linear regime at low peak fluence, the rate at which the beam size decreases with increasing fluence is lower for larger numbers of pulses, indicating weaker self-focusing. Plotting the data versus peak intensity shows similar behavior for all pulse numbers, as is to be expected (Fig. 10 (b)). Basically, self-focusing is effectively suppressed by dividing the energy among more pulses, which is a clear benefit of the pulse train approach.

3.4 Optimal focusing for maximizing THz conversion efficiency

At this point, it is interesting to investigate the question of the optimum pump beam size, considering the effect of self-focusing as well. Assuming a nondepleted pump, the efficiency of THz generation via optical rectification using a bandwidth-limited ultrashort pulse can be estimated using [47]:

$$\eta_{THz} = g_{bw}\frac{2\Omega_0^3\, d_{eff}^2\, L_{eff}}{\varepsilon_0 c^2 n_{THz}\, n_{pump}^2\, \Delta n}\frac{U_{pump}}{\pi\, w^2} = g_{bw}\frac{2\Omega_0^3\, d_{eff}^2\, L_{eff}}{\pi\varepsilon_0 c^3\, n_{pump}^2\, \Delta n}U_{pump}h(\xi) \qquad (6)$$

In Eq. 6, ε_0 is the permittivity of free space, c is the speed of light, n_{pump} is the optical refractive index at the pump wavelength, Δn is the difference between the THz-phase and optical group indices, $\Omega_0$is the central angular frequency of THz at the corresponding resonance, U_{pump} is the pump energy, L_{eff} is the effective crystal length, and $h(\xi)$ is the enhancement factor due to the pump focusing [49]. For plane waves ($\xi \ll 1$), enhancement factor reduces to the focusing parameter ($h(\xi) = \xi$) [47]. For other beam shapes, the enhancement factor could be calculated using Green's function method by integration over the nonlinear polarization distribution in real space [47,48,51]. In our simple model, we have calculated the angular amplitude distribution of our Gaussian beam [52] and calculated the performance of different Fourier components on THz phase matching and output coupling at the exit surface of the PPLN. In Fig. 11, we have plotted the calculated variation of the THz enhancement factor as a function of the focusing parameter for several cases. In Fig. 11 (a)

and (b), experimental data taken at cryogenic and room temperatures are also included, respectively. Note that, while including the experimental data, we have assumed that the data taken with the largest pump beam diameter (~4 mm) is large enough to be approximated as a plane wave.

Fig. 11 shows that, since a plane wave does not suffer from diffraction and so on, in a plane-wave model, one can enhance the THz conversion efficiency indefinitely by focusing tighter and tighter (brown solid line, which corresponds to increasing the fluence for a fixed pump energy via reducing the pump beam diameter). Then, if one takes into account the limitations of a tightly focused Gaussian wave in phase matching the PPLN crystal and out-coupling efficiency of the THz wave at the exit of the crystal, the curve starts to bend from its linear trend for focusing parameters above 1 (blue solid line in Fig. 110). Note that, these two factors are not sufficient to explain the experimental trend, which saturates much earlier.

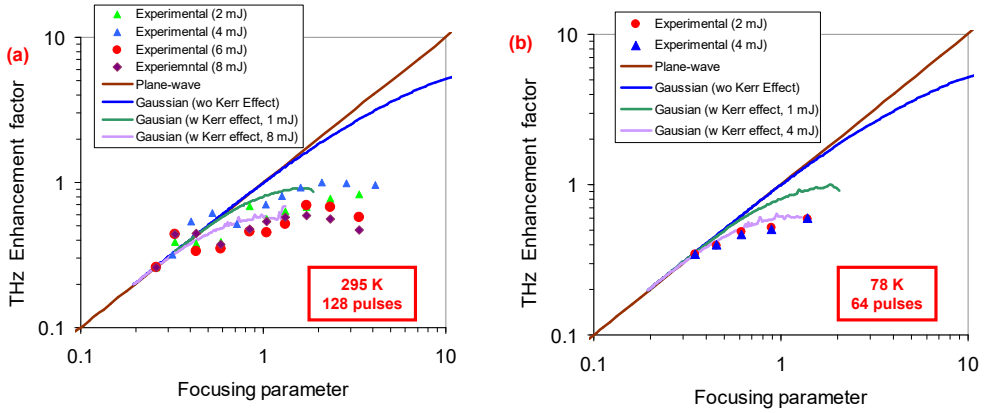

Fig. 11. Measured and calculated THz enhancement factor as a function of focusing parameter (a) at room and (b) cryogenic temperatures. The dots represent the experimental data taken at different incident pulse energies. The solid curves are numerical calculations for plane waves and Gaussian beams. The Kerr lensing effect is also considered in the numerical estimation at pulse energy values of 1 mJ and 8 mJ for RT data and 1 mJ and 4 mJ for cryogenic data, respectively.

Hence, as a further factor, we have also considered the effect of self-focusing (the Kerr effect) by modeling the Kerr effect in the PPLN crystal as a distributed thin lens (see Appendix Section 5.6). While considering the Kerr lensing effect, of course, the energy of the pulse also comes into play since it determines the energy per pulse in the pulse burst and, hence, the peak fluence of each pulse. Here, we display simulation curves at two representative pulse energies: 1 mJ and 8 mJ for RT (1 mJ and 4 mJ at 78 K). Note that, with the inclusion of the Kerr effect, the estimated THz conversion efficiency performance decreases further with focusing and starts to match the experimental trend much better. On the other hand, we have just performed a modified simple 1-D simulation here, and a detailed 3-D model that also includes other effects such as parasitic second harmonic generation, and multiphoton-induced free-carrier absorption [36,37] is required for more accurate modeling of the THz generation process.

In short, the carefully taken experimental data in this work already show that Kerr-lensing is a significant limitation in the efficiency scaling of MC THz generation. Furthermore, the pulse train excitation approach clearly reduces the strength of undesired nonlinearities, such as Kerr-lensing and SHG, by reducing the peak intensity of the pump pulses. So, excitation of the PPLN crystal with a pulse train not only reduces the bandwidth of the generated THZ but also increases the THz conversion efficiency and reduces the risk of laser-induced damage to the crystal by reducing the Kerr-lensing effect.

4. Conclusions

In conclusion, in this work, we have studied the limitations of narrowband MC THz generation via OR in PPLN crystals in detail. PPLN crystal with a poling period of 400 μm is pumped with a pulse train with 800-fs long pulses. The number of pulses in the pulse train could be adjusted between 2 and 128, and the time separation between the pulses is optimized for on-resonance excitation of the PPLN crystal at 286 GHz at 78 K and at 262 GHz at room temperature. THz generation efficiency, parasitic SHG efficiency, and variation of transmitted pump beam profile are investigated as a function of incident pump beam diameter. Our measurements showed that the usage of a small pump beam size reduces THz conversion efficiency due to the strong diffraction of the THz beam. Moreover, an investigation of the transmitted beam profiles revealed that the effect is intensified due to self-focusing. We have also demonstrated that the usage of pulse trains for excitation not only helps with the narrowing of the THz spectral width but also plays a crucial role in mitigating the effect of undesired nonlinearities, such as self-focusing and parasitic SHG, and hence provides improved THz generation efficiencies.

5. Appendix

5.1 Confirmation for internal THz conversion efficiency estimation

Our estimate of internal THz energies requires knowledge of the loss of several optical elements at THz frequencies, which could be error-prone [25]. Hence, we have investigated the spectral shift of the transmitted pump beam to validate our methodology. The measured spectral shifts of the transmitted pump at different pump peak fluences are shown in Fig. 12, both at cryogenic and room temperatures. For both cases, a net spectral shift towards longer wavelengths is clearly evident due to the loss of pump photon energy in the THz generation process.

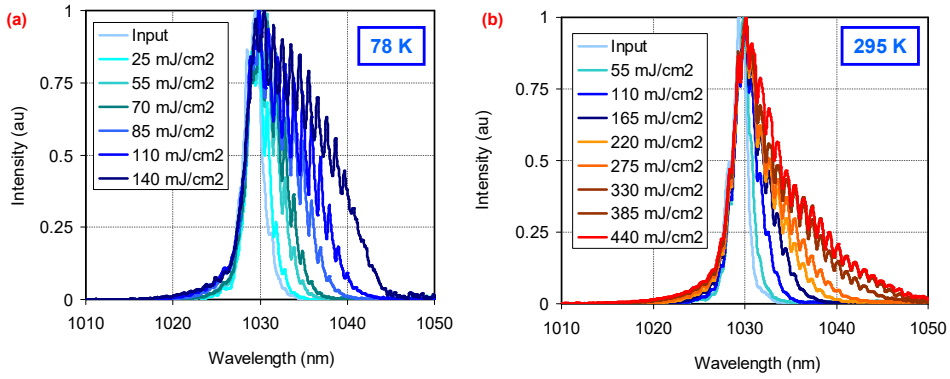

Fig. 12. Measured optical spectrum of the transmitted pump beam at different incident fluence values at (a) cryogenic (78 K) and (b) room (295 K) temperatures. The spectral shift indicates an efficiency upper bound of 0.47% at 78 K and 0.44% at 295 K, at incident fluences of 140 mJ/cm^2 and 450 mJ/cm^2, respectively.

Using the basic energy conservation principle, one can use this spectral shift data to estimate an upper bound for THz conversion efficiency. With that, we have calculated an internal THz conversion efficiency value of 0.47% at 140 mJ/cm^2 incident fluence at 78 K and an efficiency of 0.44% at 450 mJ/cm^2 incident fluence at room temperature. The efficiency value at cryogenic temperatures is close to what we have estimated for the internal THz generation efficiency (only around 10% above), indicating that at 78 K, the absorption of the lithium niobate crystal should be relatively low (as in good agreement with literature) [33]. This also indicates that within error bars (±20%), our estimation for internal THz

conversion efficiency is accurate. For the room-temperature case, the upper bound estimate for internal efficiency from spectral data (0.44%) is way above what we have measured from the system (0.045%). This indicates that most of the generated THz is absorbed within the PPLN crystal at room temperature [33].

It is also interesting to compare the difference in spectral shapes recorded at different temperatures. The spectral shift data taken at 140 mJ/cm^2 peak fluence at 78 K and spectral shift data taken at 450 mJ/cm^2 peak fluence at room temperature both indicate an internal efficiency of around 0.4-0.5%. However, the shape of the red-shifted spectra is quite different in both cases. We see a very homogeneous broadening of the optical spectra at cryogenic temperatures, compared to the asymmetric tail one observes at room temperature. This again shows that only a small portion of the generated THz at the initial portions of the PPLN crystal could reach later parts of the crystal at room temperature, and hence the number of photons that can have multiple cascading is rather low, resulting in an asymmetric spectral shift. Moreover, due to limited seeding (because of strong THz absorption), reaching a similar efficiency in the RT case requires 3 times more fluency. As a side note, the period of spectral modulation observed in the transmitted spectra agrees with the central frequency of THz generated quite well. At 78 K, a $\Delta\lambda$ of 1.025 nm is measured, which corresponds to a frequency difference of 290 GHz, and at room temperature, a $\Delta\lambda$ of 0.92 nm is observable, which corresponds to a frequency of 260 GHz.

5.2 Properties of the parasitic second harmonic generation

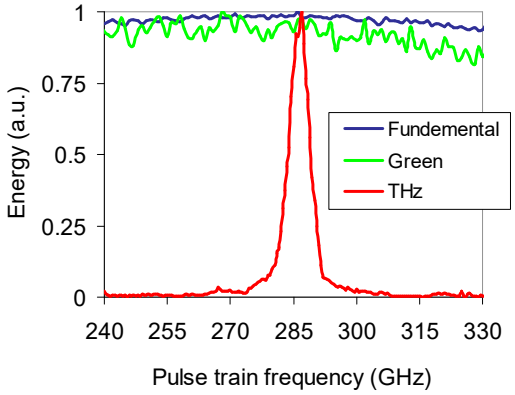

Fig. 13. Measured energy of the pump (fundamental) and parasitic second harmonic (green) as a function of pulse train frequency. For comparison, the resonant behavior of the THz energy is also shown.

In this subsection, we will provide more information on the properties of the generated parasitic second harmonic light, as to our knowledge, this has not been reported in the literature yet. As discussed earlier, the SH light is not phase-matched, and it is not resonant with the pulse train. In Fig. 13, we show the measured variation of parasitic SHG and THz energy as a function of pulse train frequency for a pulse burst consisting of 128 pulses. As we can see, there is only a weak change in the measured SHG/green efficiency, and as expected, the parasitic SHG does not show any resonance behavior. On the other hand, we see a clear resonance behavior in THz energy, as described earlier in Section 3.1. In Fig. 13, we also show the change in pump pulse energy, which reduces a little due to the non-perfect alignment of the pulse-train setup (as the frequency is tuned with 128 pulses, 7 motors in each arm move in the pulse train divider setup, and hence minor alignment issues might couple into the measurement).

We have also measured the temperature dependence of the parasitic SH energy between 78 K and 350 K. As we can see from Fig. 14 (a), within error bars, we did not observe a

significant temperature difference in parasitic SHG energy, which is expected as the process is non-phase matched, and there is not a significant change of PPLN loss around 515 nm or phase matching condition for the green process when the temperature of PPLN is changed. As a final note, in Fig. 14 (b), we show the measured optical spectrum of the generated green beam at different incident pump energy values. As we can see, the green spectrum gets broader, and its central wavelength is red-shifted as the pump energy is increased. This is also expected since the THz generation process becomes more effective at higher pump energies/fluences and this shifts the wavelengths of the pump pulses to longer wavelengths (Fig. 12 (a)), and here we see a signature of this in the generated SH spectrum as well.

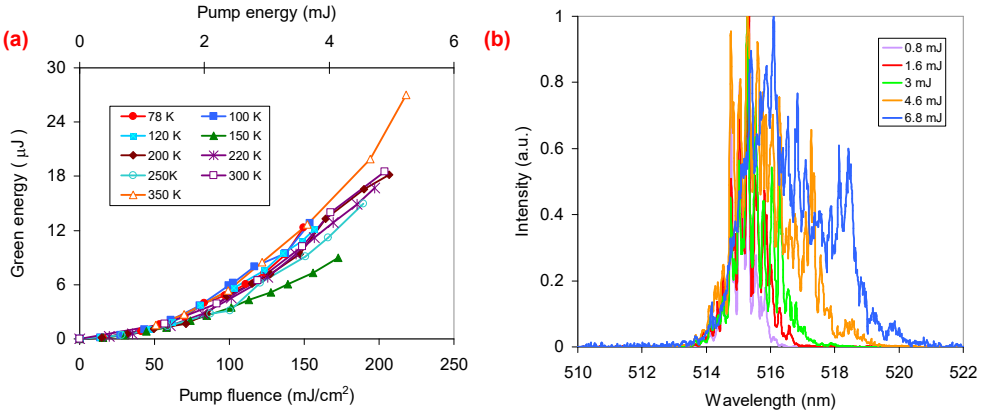

Fig.14. (a) Measured variation of parasitic second harmonic (green) energy as a function of pump fluence at selected temperatures between 78 K and 350 K. (b) Measured optical spectrum of the parasitic second harmonic (green) at room temperature for different incident pump energy levels. The data is taken with the 2 cm long PPLN crystal with a QPM period of 400 µm, using a pulse train with 64 pulses and a beam diameter of 3.5 mm.

5.3 THz and parasitic SHG efficiency as a function of crystal length at room temperature

We have also investigated the variation of THz and parasitic green generation efficiency as a function of crystal length. The data is taken at room temperature, as it is easier to swap crystals for this case. Figure 15 shows the measured variation of THz and green energy/efficiency as a function of pump burst fluence for 3 different PPLN crystals with the same polling period but different lengths of 10 mm, 20 mm, and 40 mm. We see that for all crystals, both the THz and green efficiencies saturate and even roll over. For the parasitic green, the maximum efficiencies obtained from different crystals are similar within experimental error bars. The main difference is that the optimum fluence operation for the highest green yield reduces as the crystal gets longer, which is somehow expected since the detrimental effect of the Kerr lensing on the pump beam increases with crystal length (Eq. 10). For the THz conversion efficiency, the optimum fluence also gets lower with increased crystal length. However, on top of this, we also see that the shortest crystal operates more efficiently than the long crystal. We believe that here, the difference observed between green and THz performance is due to the sensitivity of the THz beam into pump beam size owing to its much longer wavelengths and much shorter Rayleigh ranges.

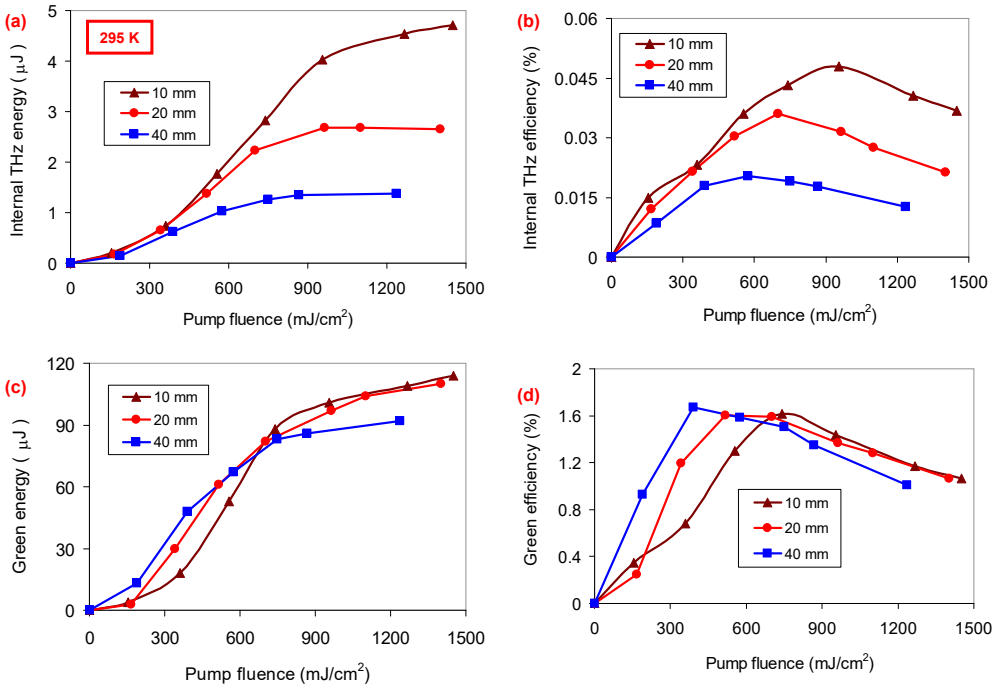

Fig. 15. Measured variation of (a) internal THz energy and (b) internal THz conversion efficiency, (c) parasitic second harmonic (green) energy, and (d) green efficiency as a function of pump fluence for 3 different PPLN crystals with lengths of 10 mm, 20 mm, and 40 mm. The data is taken at room temperature (295 K), with PPLN crystals with a QPM period of 400 μm, using a pulse train with 128 pulses.

5.6 Variation of output THz beam size with pump focusing

The THz beam size at the exit of the PPLN crystal was also studied as a function of the pump beam diameter to understand if the collection efficiency of the system is sufficient. Figure 16 shows the measured THz beam profile on the horizontal axis, at around 10 cm after the PPLN crystal's end surface. This is the place where the first 2-inch off-axis parabola was placed, and the beam size at his position is also informative on how much of the generated THz is collected. The data is taken at 78 K, using a pump burst consisting of 64 pulses. We can see from Fig. 16 that, within experimental errors, the measured THz beam shape is identical, and it does not reflect the changes in the pump beam diameter. The FWHM beam diameter is around 30 mm, and we estimate that the collection efficiency of the OAP is around 90%. We believe that, for this relatively long PPLN crystal, the crystal acts as a waveguide for the generated THz. Also, at the exit surface, any content of the THz beam that is incident at angles above the critical angle (~11.35°) is fully reflected back into the PPLN and does not contribute to the transmitted THz beam profile that is measured here. As a result, the output beam profile of the THz beam does not really change with the pump beam diameter (at least for this 4 mm x 4mm aperture PPLN crystal used here, and at these THz frequencies). It is clear that, for very tightly focused pump beams, the output coupling efficiency of the generated THz will be reduced, resulting in lower THz generation efficiencies, as we have discussed earlier in the manuscript.

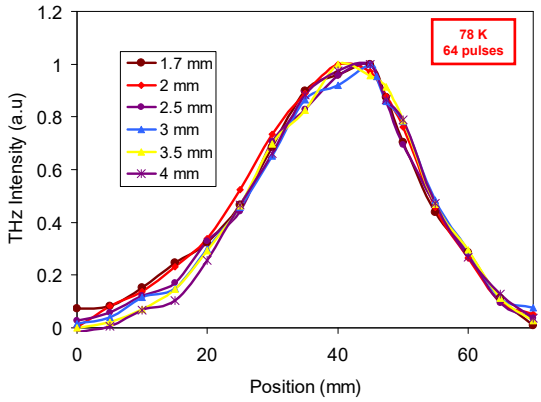

Fig.16. Measured variation of THz beam profile 10 cm after the PPLN crystal at different pump beam diameters. The data is taken at cryogenic temperatures, with the 2 cm long PPLN crystal with a QPM period of 400 μm, using a pulse train with 64 pulses.

5.6 Long-term stability of the MC THz system

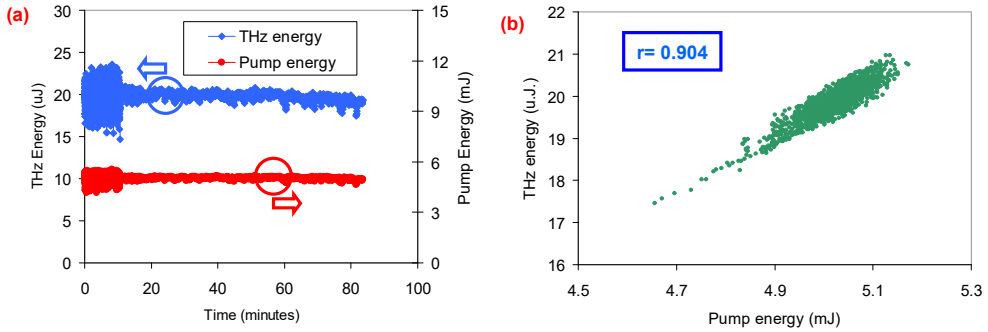

Fig. 17. (a) Measured stability of incident pump pulse and THz output energies. The first 10 minutes is a shot-to-shot measurement, and after that, an average of 10 is applied to look at the long-term variations. (b) Correlation between pump energy fluctuations and THz energy fluctuations. The Pearson correlation coefficient factor (r) is calculated to be 0.904, indicating a strong positive correlation.

We have further measured the long-term stability of the THz beam to study the presence of any mechanism that could deteriorate the long-term performance (Fig. 17 (a)) and to confirm that the fluences that are used are below the laser-induced damage threshold of the PPLN crystal at cryogenic temperatures. The first 10 minutes of data in Fig. 17 (a) shows shot-to-shot energy fluctuations in the pump laser and THz output. Analyzing the data, we found a shot-to-shot RMS energy stability of 3.95% and 5.99% for the pump and THz energies. The rest of the data in Fig. 17(a) is then taken with an averaging of 10, to better observe the long-term trends in the data. As we can see, the THz energy is almost constant, and the slow decrease of THz energy observed is due to the slow reduction in pump energy. At the peak fluence of 150 mJ/cm^2 we have applied while taking data in Fig. 17, we have not observed any damage to the PPLN crystal, which shows that this is a relatively safe fluence for long-term operation of PPLN at cryogenic temperatures (at least for the burst length used here, which was around 200 ps long, and at the repetition rate of 10 Hz). In Fig 17 (b), we show the correlation between pump and THz energy. As we can see, the fluctuations in THz energy are strongly correlated with the pump energy fluctuations, and the Pearson correlation

coefficient factor is as high as 0.904. During these measurements, a big part of the setup was not covered, resulting in relatively large fluctuations in pump energy which manifested itself also in THz energy. We believe that in future studies using more stable amplifiers, the shot-to-shot rms noise in THz energy could easily be reduced below the 1% level [53].

5.6 Distributed thin-lens mode for Kerr Medium

Here, we will briefly summarize the model we used to simulate the Kerr effect in lithium niobate. Complex q-parameter description of Gaussian beams enables easy calculation of its properties as it propagates through optical elements as a simple bilinear transformation, and it is also used in our analysis. This requires knowledge of the ABCD matrix of the optical elements through which the Gaussian beam propagates. The propagation of a Gaussian beam through a Kerr media could also be approximately modeled using ABCD matrix formalism by ignoring the higher-order terms in its lateral intensity distribution. It can be shown that the ABCD matrix of a Kerr medium can be written as [54]:

$$ABCD_{Kerr} = \begin{bmatrix} cos(\gamma l) & \frac{1}{\bar{n}} sin(\gamma l) \\ -\bar{n}\,\gamma Sin(\gamma l) & cos(\gamma l) \end{bmatrix}, \tag{7}$$

where the parameters are defined as:

$$\bar{n} = n + n_2\, I \tag{8}$$

$$\gamma = \sqrt{\frac{8\, n_2\, P}{\pi\, \bar{n}}} \frac{1}{w^2} \tag{9}$$

Above, n is the usual, weak-field refractive index at the pump wavelength, n_2 is the nonlinear refractive index of the Kerr medium, I is the peak intensity of the Gaussian pulse, P is the peak power, l is the length of the Kerr medium, and w is the Gaussian beam radius. In the ABCD matrix, element C describes the lensing behavior (C=- 1/f), and in the case of weak Kerr lensing, we can approximate the Kerr-lensing strength (f_{kerr}) as $1/(\bar{n}\,\gamma^2 l)$. Then the Kerr lens diopter power can be rewritten as:

$$f_{kerr}^{-1} = \frac{8\, n_2\, P\, l}{\pi\, w^4}\ . \tag{10}$$

From Eq. 10, we see that the Kerr lens strength scales linearly with the nonlinear refractive index of the medium, with the crystal length, and with the peak power of the pulses. On the other hand, it scales with w^{-4}, showing its very strong dependence on the initial beam size.

While using the ABCD formalism, since our PPLN crystal is rather long/thick, taking it as a single element (thin lens) will not provide a correct answer since the incident beam will start to focus inside the PPLN crystal, and this will increase the peak powers and the effective Ker lens[55]. Hence, here we have applied a distributed Kerr lens model (e.g. see Fig. 3 in [55]), where we have divided the PPLN crystal into many pieces (>100), and the output of the nth piece is used as an input to the n+1th piece to acquire a more trustable estimation of the Kerr lensing behavior. In the analysis, the nonlinear refractive index of lithium niobate is taken as 9.1×10^{-20} m^2/W [50,56].

Funding

Seventh Framework Programme (FP7) FP7/2007- 2013 European Research Council (ERC) Synergy Grant (609920). Deutsche Forschungsgemeinschaft (Project No. 405983224). Deutsches Electronen-Synchrotron (POV-IV – Matter MML-DMC).

Data Availability

Data underlying the results presented in this paper are not publicly available at this time but may be obtained from the authors upon reasonable request.

Disclosures

The authors declare no conflicts of interest.

References

1. G. L. Dakovski, W.-S. Lee, D. G. Hawthorn, N. Garner, D. Bonn, W. Hardy, R. Liang, M. C. Hoffmann, en J. J. Turner, "Enhanced coherent oscillations in the superconducting state of underdoped YBaCuO6+x induced via ultrafast terahertz excitation," Phys. Rev. B **91**(22), 220506 (2015).
2. E. A. Nanni, W. R. Huang, K.-H. Hong, K. Ravi, A. Fallahi, G. Moriena, R. J. Dwayne Miller, en F. X. Kärtner, "Terahertz-driven linear electron acceleration," Nat. Commun. **6**(1), 8486 (2015).
3. M. Bass, P. A. Franken, J. F. Ward, en G. Weinreich, "Optical Rectification," Phys. Rev. Lett. **9**(11), 446–448 (1962).
4. K. Uchida, H. Hirori, T. Aoki, C. Wolpert, T. Tamaya, K. Tanaka, T. Mochizuki, C. Kim, M. Yoshita, H. Akiyama, L. N. Pfeiffer, en K. W. West, "Time-resolved observation of coherent excitonic nonlinear response with a table-top narrowband THz pulse wave," Appl. Phys. Lett. **107**(22), 221106 (2015).
5. C. Vicario, A. Trisorio, S. Allenspach, C. Rüegg, en F. Giorgianni, "Narrow-band and tunable intense terahertz pulses for mode-selective coherent phonon excitation," Appl. Phys. Lett. **117**(10), 101101 (2020).
6. E. Rowe, B. Yuan, M. Buzzi, G. Jotzu, Y. Zhu, M. Fechner, M. Först, B. Liu, D. Pontiroli, M. Riccò, en A. Cavalleri, "Resonant enhancement of photo-induced superconductivity in K3C60," Nat. Phys. **19**(12), 1821–1826 (2023).
7. A. S. Disa, M. Fechner, T. F. Nova, B. Liu, M. Först, D. Prabhakaran, P. G. Radaelli, en A. Cavalleri, "Polarizing an antiferromagnet by optical engineering of the crystal field," Nat. Phys. **16**(9), 937–941 (2020).
8. P. D. Cunningham en L. M. Hayden, "Optical properties of DAST in the THz range," Opt. Express **18**(23), 23620–23625 (2010).
9. A. Schneider, M. Neis, M. Stillhart, B. Ruiz, R. U. A. Khan, en P. Günter, "Generation of terahertz pulses through optical rectification in organic DAST crystals: theory and experiment," J. Opt. Soc. Am. B **23**(9), 1822–1835 (2006).
10. L. Mutter, F. D. Brunner, Z. Yang, M. Jazbinšek, en P. Günter, "Linear and nonlinear optical properties of the organic crystal DSTMS," J. Opt. Soc. Am. B **24**(9), 2556–2561 (2007).
11. S.-J. Kwon, M. Jazbinsek, O.-P. Kwon, en P. Günter, "Crystal Growth and Morphology Control of OH1 Organic Electrooptic Crystals," Cryst. Growth Des. **10**(4), 1552–1558 (2010).
12. C. Vicario, M. Jazbinsek, A. V Ovchinnikov, O. V Chefonov, S. I. Ashitkov, M. B. Agranat, en C. P. Hauri, "High efficiency THz generation in DSTMS, DAST and OH1 pumped by Cr:forsterite laser," Opt. Express **23**(4), 4573–4580 (2015).
13. M. Jazbinsek, U. Puc, A. Abina, en A. Zidansek, "Organic Crystals for THz Photonics," Appl. Sci. **9**(5), (2019).
14. S. Mansourzadeh, T. Vogel, A. Omar, T. O. Buchmann, E. J. R. Kelleher, P. U. Jepsen, en C. J. Saraceno, "Towards intense ultra-broadband high repetition rate terahertz sources based on organic crystals [Invited]," Opt. Mater. Express **13**(11), 3287–3308 (2023).
15. B. Liu, H. Bromberger, A. Cartella, T. Gebert, M. Först, en A. Cavalleri, "Generation of narrowband, high-intensity, carrier-envelope phase-stable pulses tunable between 4 and 18 THz," Opt. Lett. **42**(1), 129–131 (2017).
16. L. E. Zapata, M. Pergament, M. Schust, S. Reuter, J. Thesinga, C. Zapata, M. Kellert, U. Demirbas, A.-L. Calendron, Y. Liu, en F. X. Kärtner, "One-joule 500-Hz cryogenic Yb:YAG laser driver of composite thin-disk design," Opt. Lett. Vol. 47, Issue 24, pp. 6385-6388 **47**(24), 6385–6388 (2022).
17. Y.-S. Lee, T. Meade, V. Perlin, H. Winful, T. B. Norris, en A. Galvanauskas, "Generation of narrow-band terahertz radiation via optical rectification of femtosecond pulses in periodically poled lithium niobate," Appl. Phys. Lett. **76**(18), 2505–2507 (2000).
18. Y.-S. Lee, T. Meade, M. DeCamp, T. B. Norris, en A. Galvanauskas, "Temperature dependence of narrow-band terahertz generation from periodically poled lithium niobate," Appl. Phys. Lett. **77**(9), 1244–1246

(2000).
19. Y.-S. Lee, N. Amer, en W. C. Hurlbut, "Terahertz pulse shaping via optical rectification in poled lithium niobate," in *Conference on Lasers and Electro-Optics/Quantum Electronics and Laser Science Conference*, Technical Digest (Optica Publishing Group, 2003), bl QWB3.
20. C. Zhang, Y. Avetisyan, G. Abgaryan, I. Kawayama, H. Murakami, en M. Tonouchi, "Tunable narrowband terahertz generation in lithium niobate crystals using a binary phase mask," Opt. Lett. **38**(6), 953–955 (2013).
21. A. G. Stepanov, J. Hebling, en J. Kuhl, "Generation, tuning, and shaping of narrow-band, picosecond THz pulses by two-beam excitation," Opt. Express **12**(19), 4650–4658 (2004).
22. J. Ahn, A. V Efimov, R. D. Averitt, en A. J. Taylor, "Terahertz waveform synthesis via optical rectification of shaped ultrafast laser pulses," Opt. Express **11**(20), 2486–2496 (2003).
23. S. W. Jolly, N. H. Matlis, F. Ahr, V. Leroux, T. Eichner, A.-L. Calendron, H. Ishizuki, T. Taira, F. X. Kärtner, en A. R. Maier, "Spectral phase control of interfering chirped pulses for high-energy narrowband terahertz generation," Nat. Commun. **10**(1), 2591 (2019).
24. H. T. Olgun, W. Tian, G. Cirmi, K. Ravi, C. Rentschler, H. Çankaya, M. Pergament, M. Hemmer, Y. Hua, D. N. Schimpf, N. H. Matlis, en F. X. Kärtner, "Highly efficient generation of narrowband terahertz radiation driven by a two-spectral-line laser in PPLN," Opt. Lett. **47**(10), 2374–2377 (2022).
25. N. H. Matlis, Z. Zhang, U. Demirbas, C. Rentschler, K. Ravi, M. Youssef, G. Cirmi, M. Pergament, M. Edelmann, S. M. Mohamadi, S. Reuter, en and F. X. Kärtner, "Precise parameter control of multicycle terahertz generation in PPLN using flexible pump pulse trains," Opt. Express **31**(26), 44424–44443 (2023).
26. J. A. L'huillier, G. Torosyan, M. Theuer, C. Rau, Y. Avetisyan, en R. Beigang, "Generation of THz radiation using bulk, periodically and aperiodically poled lithium niobate – Part 2: Experiments," Appl. Phys. B **86**(2), 197–208 (2007).
27. Y. S. Lee, T. Meade, T. B. Norris, en A. Galvanauskas, "Tunable narrow-band terahertz generation from periodically poled lithium niobate," Appl. Phys. Lett. **78**(23), 3583–3585 (2001).
28. K. Ravi, D. N. Schimpf, en F. X. Kärtner, "Pulse sequences for efficient multi-cycle terahertz generation in periodically poled lithium niobate," Opt. Express **24**(22), 25582–25607 (2016).
29. K. Ravi en F. X. Kärtner, "Raman Shifting Induced by Cascaded Quadratic Nonlinearities for Terahertz Generation," Laser Photon. Rev. **14**(11), 2000109 (2020).
30. F. Ahr, S. W. Jolly, N. H. Matlis, S. Carbajo, T. Kroh, K. Ravi, D. N. Schimpf, J. Schulte, H. Ishizuki, T. Taira, A. R. Maier, en F. X. Kärtner, "Narrowband terahertz generation with chirped-and-delayed laser pulses in periodically poled lithium niobate," Opt. Lett. **42**(11), 2118–2121 (2017).
31. F. Ahr, K. Ravi, S. Carbajo, S. Jolly, T. Kroh, D. Schimpf, N. Matlis, A. R. Maier, en F. X. Kärtner, "Pulse-train pumping for efficient narrowband terahertz generation in periodically poled lithium niobate," in *Conference on Lasers and Electro-Optics*, OSA Technical Digest (online) (Optica Publishing Group, 2016), bl JTh2A.58.
32. D. N. Schimpf, H. T. Olgun, A. Kalaydzhyan, Y. Hua, N. H. Matlis, en F. X. Kärtner, "Frequency-comb-based laser system producing stable optical beat pulses with picosecond durations suitable for high-precision multi-cycle terahertz-wave generation and rapid detection," Opt. Express, Vol. 27, Issue 8, pp. 11037-11056 **27**(8), 11037–11056 (2019).
33. U. Demirbas, C. Rentschler, Z. Zhang, M. Pergament, N. H. Matlis, en F. X. Kärtner, "Temperature dependence of THz generation efficiency, THz refractive index, and THz absorption in lithium-niobate around 275 GHz," Opt. Mater. Express **14**(7), 1886–1900 (2024).
34. S. B. Bodrov, I. E. Ilyakov, B. V Shishkin, en A. N. Stepanov, "Efficient terahertz generation by optical rectification in Si-LiNbO3-air-metal sandwich structure with variable air gap," Appl. Phys. Lett. **100**(20), 201114 (2012).
35. S. B. Bodrov, I. E. Ilyakov, B. V Shishkin, en M. I. Bakunov, "Highly efficient Cherenkov-type terahertz generation by 2-μm wavelength ultrashort laser pulses in a prism-coupled LiNbO3 layer," Opt. Express **27**(25), 36059–36065 (2019).
36. I. Benabdelghani, G. Tóth, G. Krizsán, G. Bazsó, Z. Szaller, N. Mbithi, P. Rácz, P. Dombi, G. Polónyi, en J. Hebling, "Three-photon and four-photon absorption in lithium niobate measured by the Z-scan technique," Opt. Express **32**(5), 7030–7043 (2024).
37. S.-C. Zhong, Z.-H. Zhai, J. Li, L.-G. Zhu, J. Li, K. Meng, Q. Liu, L.-H. Du, J.-H. Zhao, en Z.-R. Li, "Optimization of terahertz generation from LiNbO3 under intense laser excitation with the effect of three-photon absorption," Opt. Express **23**(24), 31313–31323 (2015).
38. K. Ravi, W. R. Huang, S. Carbajo, E. A. Nanni, D. N. Schimpf, E. P. Ippen, en F. X. Kärtner, "Theory of terahertz generation by optical rectification using tilted-pulse-fronts," Opt. Express **23**(4), 5253–5276 (2015).
39. X. Zhu, D. R. Bacon, J. Madéo, en K. M. Dani, "High Field Single- to Few-Cycle THz Generation with Lithium Niobate," Photonics **8**(6), (2021).
40. T. Kroh, T. Rohwer, D. Zhang, U. Demirbas, H. Cankaya, M. Hemmer, Y. Hua, L. E. Zapata, M. Pergament, F. X. Kärtner, en N. H. Matlis, "Parameter sensitivities in tilted-pulse-front based terahertz setups and their implications for high-energy terahertz source design and optimization," Opt. Express **30**(14), 24186–24206 (2022).
41. T. Kroh, T. Rohwer, L. Wang, U. Demirbas, H. Cankaya, M. Pergament, F. X. Kärtner, en N. H. Matlis,

"Robust optimization of single-cycle THz setups based on phase-matching via tilted pulse fronts using an incident-fluence metric," **11264**(2), 1126416 (2020).
42. C. Rentschler, N. H. Matlis, U. Demirbas, Z. Zhang, M. Pergament, A. Zukauskas, C. Canalias, H. Ishizuki, V. Pasiskevicius, F. Laurell, T. Taira, en F. X. Kärtner, "Parameter dependencies in multicycle THz generation with tunable high-energy pulse trains in large-aperture crystals," in *Proc.SPIE* (2024), **12869**, bl 128690M.
43. Y. Furukawa, K. Kitamura, A. Alexandrovski, R. K. Route, M. M. Fejer, en G. Foulon, "Green-induced infrared absorption in MgO doped LiNbO3," Appl. Phys. Lett. **78**(14), 1970–1972 (2001).
44. R. G. Batchko, G. D. Miller, A. Alexandrovski, M. M. Fejer, en R. L. Byer, "Limitations of high-power visible wavelength periodically poled lithium niobate devices due to green-induced infrared absorption and thermal lensing," in *Technical Digest. Summaries of Papers Presented at the Conference on Lasers and Electro-Optics. Conference Edition. 1998 Technical Digest Series, Vol.6 (IEEE Cat. No.98CH36178)* (1998), bll 75–76.
45. U. Demirbas, C. Rentschler, Z. Zhang, M. Pergament, N. H. Matlis, en F. X. Kärtner, "Two-dimensional effects in Multicycle THz generation with tunable pump pulse trains in lithium niobate," in *2023 48th International Conference on Infrared, Millimeter, and Terahertz Waves (IRMMW-THz)* (2023), bll 1–2.
46. J. R. Morris en Y. R. Shen, "Theory of far-infrared generation by optical mixing," Phys. Rev. A **15**(3), 1143–1156 (1977).
47. K. L. Vodopyanov, "Optical generation of narrow-band terahertz packets in periodically-inverted electro-optic crystals: conversion efficiency and optimal laser pulse format," Opt. Express **14**(6), 2263–2276 (2006).
48. Y. R. Shen, "Far-infrared generation by optical mixing," Prog. Quantum Electron. **4**, 207–232 (1976).
49. G. D. Boyd en D. A. Kleinman, "Parametric Interaction of Focused Gaussian Light Beams," J. Appl. Phys. **39**(8), 3597–3639 (1968).
50. R. DeSalvo, A. A. Said, D. J. Hagan, E. W. Van Stryland, en M. Sheik-Bahae, "Infrared to ultraviolet measurements of two-photon absorption and n/sub 2/ in wide bandgap solids," IEEE J. Quantum Electron. **32**(8), 1324–1333 (1996).
51. S. Guha, "Focusing dependence of the efficiency of a singly resonant optical parametric oscillator," Appl. Phys. B **66**(6), 663–675 (1998).
52. P. Malara, P. Maddaloni, G. Mincuzzi, S. De Nicola, en P. De Natale, "Non-collinear quasi phase matching and annular profiles in difference frequency generation with focused Gaussian beams," Opt. Express **16**(11), 8056–8066 (2008).
53. U. Demirbas, M. Kellert, J. Thesinga, Y. Hua, S. Reuter, M. Pergament, en F. X. Kärtner, "Highly efficient cryogenic Yb:YLF regenerative amplifier with 250 W average power," Opt. Lett. **46**(16), 3865–3868 (2021).
54. A. Penzkofer, M. Wittmann, E. Sigert, en S. MacNamara, "Kerr lens effects in a folded-cavity four-mirror linear resonator," Opt. Quantum Electron. **28**, 423–442 (1996).
55. M. Sheik-Bahae, A. A. Said, D. J. Hagan, M. J. Soileau, en E. W. Van Stryland, "Nonlinear refraction and optical limiting in thick media," Opt. Eng. **30**(8), 1228–1235 (1991).
56. K. L. Vodopyanov, "Optical THz-wave generation with periodically-inverted GaAs," Laser Photon. Rev. **2**(1–2), 11–25 (2008).